This is an author-created, un-copyedited version of an article accepted for publication/published in *Measurement Science and Technology*. IOP Publishing Ltd is not responsible for any errors or omissions in this version of the manuscript or any version derived from it. The Version of Record is available online at doi: 10.1088/0957-0233/27/12/124016 ". Posted with permission.

Reconstruction of In-Plane Strain Maps using Hybrid Dense Sensor Network composed of Sensing Skin

Austin Downey[1], Simon Laflamme[1,2] and Filippo Ubertini[3]

1 Department of Civil, Construction, and Environmental Engineering, Iowa State University, Ames, IA, USA;

2 Department of Electrical and Computer Engineering, Iowa State University, Ames, IA, USA;

3 Department of Civil and Environmental Engineering, University of Perugia, Perugia, Umbria, Italy;

E-mail: `adowney2@iastate.edu`

October 2016

Abstract.

The authors have recently developed a soft-elastomeric capacitive (SEC)-based thin film sensor for monitoring strain on mesosurfaces. Arranged in a network configuration, the sensing system is analogous to a biological skin, where local strain can be monitored over a global area. Under plane stress conditions, the sensor output contains the additive measurement of the two principal strain components over the monitored surface. In applications where the evaluation of strain maps are useful, in structural health monitoring for instance, such signal must be decomposed into linear strain components along orthogonal directions. Previous work has led to an algorithm that enabled such decomposition by leveraging a dense sensor network configurations with the addition of assumed boundary conditions. Here, we significantly improve the algorithm's accuracy by leveraging mature off-the-shelf solutions to create a hybrid dense sensor network (HDSN) to improve on the boundary condition assumptions. The system's boundary conditions are enforced using unidirectional RSGs and assumed virtual sensors. Results from an extensive experimental investigation demonstrate the good performance of the proposed algorithm and its robustness with respect to sensors' layout. Overall, the proposed algorithm is seen to effectively leverage the advantages of a hybrid dense network for application of the thin film sensor to reconstruct the surface strain fields over large surfaces.

Keywords: structural health monitoring, capacitive-based sensor, soft elastomeric capacitor, flexible membrane sensor, sensor network, signal decomposition, strain measurement.

1. Introduction

Structural health monitoring (SHM) is the automation of damage detection, localization, and prognosis of structural systems or components. The monitoring of large-scale

systems, here termed mesosystems, is especially challenging due to the inherent geometric size and complexity [1]. Mesosystems, including aerospace structures, energy systems and civil infrastructures are traditionally inspected and maintained via time-based or breakdown-based maintenance strategies. The use of SHM to enable condition-based maintenance (CBM) may lead to strong economic benefits for owners, operators, and society. Of particular interest is the field of wind energy system, where CBM is known to have substantial economic benefits [2, 3, 4].

Monitoring solutions for mesoscale structures need to be capable of global (e.g., loss of stiffness, changing boundary conditions) and local (e.g., localizing material failure, crack propagation, and fastener loosening) condition assessment over strategic locations. However, distinguishing a localized change in a structure from a global change is difficult using existing technologies and methods [5, 6]. The task is often complicated by the dependence of sensor signals on environmental effects such as temperature and humidity [7, 8]. The ability to monitor local damage over a global scale necessitates a large array of sensors [9]. However, the cost incurred in using traditional sensors can be hard to financially justify [10].

A solution to the local-global monitoring challenge involves the utilization of flexible skin-like membranes. Such films, often termed electronic artificial skins, e-skins, or sensing skins are thin electronic sheets that mimic biological skin. Research on sensing skin has recently gained popularity with advances in the field of flexible electronics [1, 11]. Dense sensor network applications of skin sensors have also been reported. Lee et al. [12] demonstrated a flexible capacitive tactile sensor. Experimentally verified using a 16×16 array of tactile cells, this artificial skin has a spatial resolution of 1 mm. Xu et al. [13] utilized a 36-sensor array of resistive heating elements on a flexible polyimide film to measure shear stress topography and flow separation on the leading edge of a delta-wing structure during wind tunnel tests. Recently, research has progressed towards microelectromechanical systems (MEMS) based flexible skins without the need for rigid packages [14, 15]. Large sensing sheets of strain gauges with embedded processors on a 50 μm thick polyimide sheet have been proposed, with applications to crack detection and localization [16, 17].

The use of resistance-based thin-film strain sensors fabricated with carbon nanotubes has attracted considerable attention in the last decade. Examples of such sensors include a strain sensor fabricated from single-walled carbon nanotubes (SWCNT) exhibiting a gauge factor between 1 and 5 [18], a highly sensitive sensor also using SWCNT but resulting in a gauge factor of 269 [19]. Advanced methods for constructing flexible membranes reinforced with self-assembled arrays of SWCNT have been investigated [20] and show great potential for the development of robust sensing skins. Transparent elastic conductors capable of transducing strain and pressure, essential in certain electronic and optoelectronic applications, have been fabricated with conductivities as high as 2,200 S/cm in the stretched state [21]. Integrated sensor-electronic have been developed from SWCNT-polymer composite patterned onto a flexible polyimide substrate using optical lithography yielding a gauge factor of 0.77 and

a resolution of 50 $\mu\varepsilon$ [22]. Strain transducers based on SWCNT have been demonstrated for measuring high strain applications, up to 280%, such as that needed for human-motion detection [23].

Capacitive-based sensing skins have also been studied for measuring strain [24], pressure [25], triaxial force [26], and humidity [27]. Capacitive-based sensors offer the potential to be highly applicable to mesoscale monitoring as they are less affected by temperature changes and can be manufactured using various techniques, including high-speed offset lithography printing process [28]. The challenge in the fabrication of sensing skins for mesosensing lies in the selection of an inexpensive polymer mix that is robust to environmental conditions [29]. In the same framework of low-cost sensing skins for mesoscale systems, the authors have previously developed a soft elastomeric capacitor (SEC). The proposed SEC was designed to be inexpensive with an easily scalable manufacturing process [30]. The SEC is fabricated from an inexpensive nanocomposite based on a styrene-co-ethylene-co-butylene-co-styrene (SEBS) block co-polymer matrix filled with titania (dielectric) and carbon black (electrodes) particles and is customizable in shape and size [31, 32]. Static [31] and dynamic behaviors [1, 33] have been characterized, including damage detection applications in wind turbine blades [34] subjected to random wind loading [35], and the effectiveness of a dense sensor network for detecting fatigue cracks has been demonstrated [36].

A particular feature of the SEC is that it measures additive in-plane strain, instead of a traditional measurement of the linear strain along a single direction. When used in a dense sensor network (DSN) the SEC is able to monitor local additive strain over large areas. Therefore, the signal can be used to reconstruct strain maps, provided that the additive strain is decomposed into linear strain components along two orthogonal directions. The authors presented an algorithm in [37] designed to leverage a DSN configuration to enable strain field decomposition. The algorithm assumed a shape function and classical Kirchhoff plate theory and solved for the coefficients of the shape function using the least squares estimator (LSE). Numerical simulations showed the promise of the algorithm. However, the proposed technique was limited by sensor placement along the edge of the plate, and the quality of the assumptions on the boundary conditions. It follows that boundary conditions can be difficult to assume for complex geometries and may be time-varying over the monitored structure' lifetime.

In this work, the authors propose a hybrid DSN (HDSN) to alleviate limitations of the previously proposed strain decomposition algorithm [37]. The HDSN considered here introduces resistive strain gauges (RSGs), a mature sensing technology capable of precise point measurements. However, due to their size, as well as technical and economic constraints, RSGs lack the ability to efficiently cover mesosurfaces [38]. The HDSN presented here combines the SECs coverage capacity with the high precision measurements of RSGs. The LSE algorithm discussed above is expanded to include RSG readings and virtual sensing nodes at known boundary conditions. The enhanced LSE algorithm also introduces weighted matrices to the LSE algorithm to concatenate data, allowing for the enforcement of localized strain conditions and the fusion of

unidirectional and additive strain sensors. The proposed strain decomposition algorithm is experimentally verified utilizing an HDSN consisting of 20 SECs and a variable number of RSGs, from 2 to 46, on a thin composite plate.

The paper is organized as follows. Section 2 provides a background on the SEC technology, including its electro-mechanical model and derivation of the prior LSE-based strain decomposition algorithm. Section 3 extends the algorithm to HDSN formulations. Section 4 illustrates the methodology used in the evaluation and validation of the algorithm. Section 5 reports and discusses algorithm results. Section 6 concludes the paper.

2. Background

The SEC, shown in figure 1(a), is a soft electronic element that transduces a change in the geometry (i.e. strain) into a change in capacitance. The fabrication process of the SEC is documented in [1]. Briefly, its dielectric is composed of an SEBS block co-polymer matrix filled with titania to increase both its permittivity and durability. Both of its conductive plates are also fabricated from an SEBS, but this time filled with carbon black particles. All of the components used in the fabrication process are readily and widely available, and its fabrication process is relatively simple. It results that the SEC is a highly scalable skin sensor. In this section, the electro-mechanical model of the SEC is derived and validated, and the basic strain decomposition algorithm previously developed by the authors reviewed.

2.1. Electro-Mechanical Model

The SEC is designed to measure in-plane strain ($x - y$ plane in figure 2(b)) and is adhered to the monitored substrate using an off-the-shelf epoxy along the $x - y$ plane. The sensor is typically installed after some pre-stretching to prevent any warping of the sensor under compressive loading of the monitored substrate. Assuming a relatively low sampling rate (< 1 kHz), the SEC can be modeled as a non-lossy capacitor with capacitance C, given by the parallel plate capacitor equation,

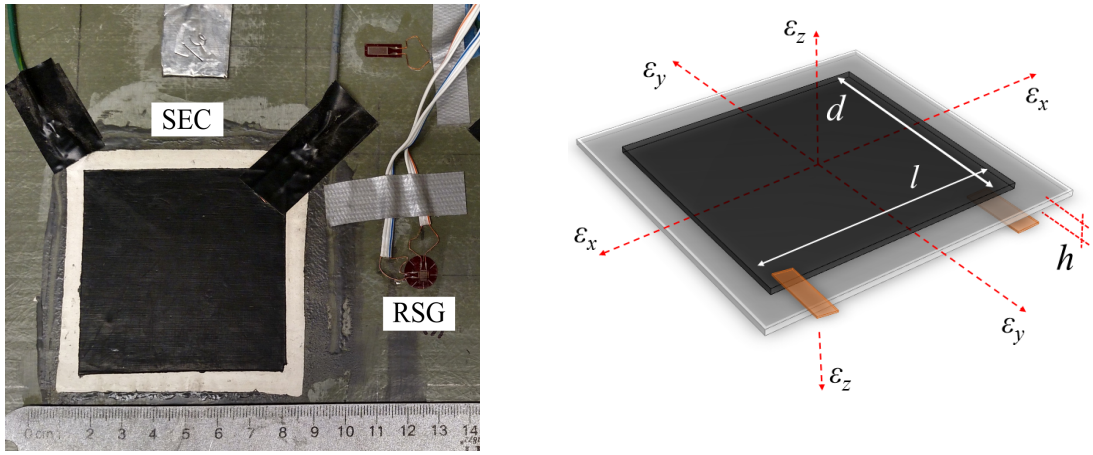

(a) (b)

Figure 1. (a) Picture of an SEC sensor compared with an RSG; and (b) sketch of an SEC's geometry with reference axes.

$$C = e_0 e_r \frac{A}{h} \tag{1}$$

where $e_0 = 8.854$ pF/m is the vacuum permittivity, e_r is the polymer relative permittivity, $A = d \cdot l$ is the sensor area of width d and length l, and h is the thickness of the dielectric. Assuming small strain, the differential of equation (1) is expressed as

$$\frac{\Delta C}{C} = \left(\frac{\Delta l}{l} + \frac{\Delta d}{d} - \frac{\Delta h}{h} \right) = \varepsilon_x + \varepsilon_y - \varepsilon_z \tag{2}$$

where ε_x, ε_y and ε_z are linear strains in the x, y and z directions as shown in figure 2(b). An expression relating ε_z to ε_x and ε_y can be obtained using Hooke's law for plane stress

$$\varepsilon_z = -\frac{\nu}{1-\nu}(\varepsilon_x + \varepsilon_y) \tag{3}$$

which gives

$$\frac{\Delta C}{C} = \lambda(\varepsilon_x + \varepsilon_y) \tag{4}$$

with

$$\lambda = \frac{1}{1-\nu} \tag{5}$$

representing the gauge factor of the sensor. For SEBS, $\nu \approx 0.49$ [39], which gives a gauge factor $\lambda \approx 2$. Equation (4) shows that the signal of the SEC varies as a function of the additive strain $\varepsilon_x + \varepsilon_y$. The linearity of the derived electro-mechanical model holds for mechanical responses up to 15 Hz [1]. An altered electro-mechanical model has been derived in [33] for modeling mechanical responses up to 40 Hz, but is not shown here for brevity.

2.2. Model Validation

The SEC's electro-mechanical model has been validated at numerous occasions. A typical result is presented here. The test setup consists of a simply supported aluminum plate of dimensions 200 x 75 x 3 mm^3 subjected to a four-point load setup to provide a constant strain field across the SEC, mounted onto the bottom surface of the plate at half-length. The performance of the SEC is validated using an off-the-shelf resistive strain gauge (RSG) (Vishay Micro-Measurements, CEA-06-500UW-120) having a resolution of 1 $\mu\varepsilon$. A quasi-static triangular load is applied using a servo-hydraulic fatigue testing machine (MTS). Data from the SECs are acquired using an inexpensive off-the-shelf data acquisition system (ACAM PCap01) sampled at 95.4 Hz. Data from the RSGs are measured using Hewlett-Packard 3852 data acquisition system at a sampling frequency of 55Hz. A time series of the measured responses of the SEC and RSG is plotted in figure 2a, where the signal of the SEC was converted into strain using the electro-mechanical model (equation (4)) specialized for uni-directional strain. Figure 2b is a plot of the measured strain from the SEC versus the applied strain. Results show a good agreement of the SEC data with the RSG data, and that the electro-mechanical model holds. The resolution of the sensor using this particular data acquisition setup is 25 μm.

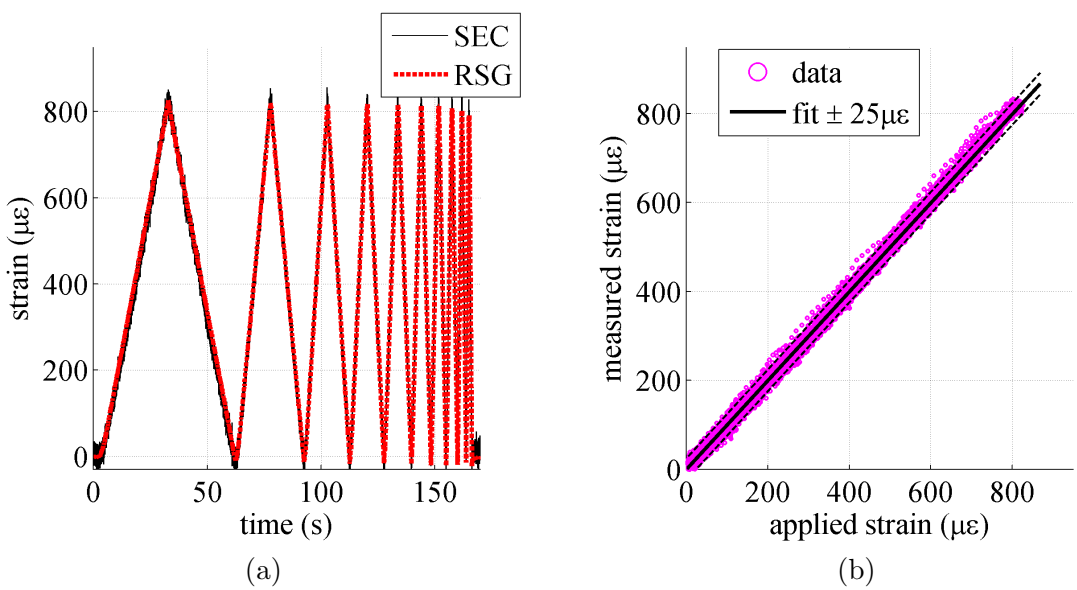

Figure 2. (a) Comparison of strain time histories for the SEC and the RSG; and (b) measured strain by the SEC versus applied strain.

2.3. Strain Decomposition Algorithm

A strain decomposition algorithm was proposed in [37] to decompose the SEC signal (equation (4)) into linear strain components in two orthogonal directions. It is summarized in this subsection and later enhanced for HDSN applications.

The algorithm consists of assuming a parametric displacement shape function, from

which the equations mapping strain in two orthogonal directions, x and y, are derived. An LSE is then used to estimate the coefficients of strain maps that would best fit the signals of the SECs, which is done after enforcing boundary conditions. A polynomial displacement shape function has shown promise for conducting strain decomposition on a thin plate. Consider a cantilever plate of the type illustrated in figure 3 and an nth order polynomial to approximate its deflection shape $w(x, y)$ as

$$w\left(x, y\right) = \sum_{i=1,j=0}^{n} b_{ij} x^i y^j \tag{6}$$

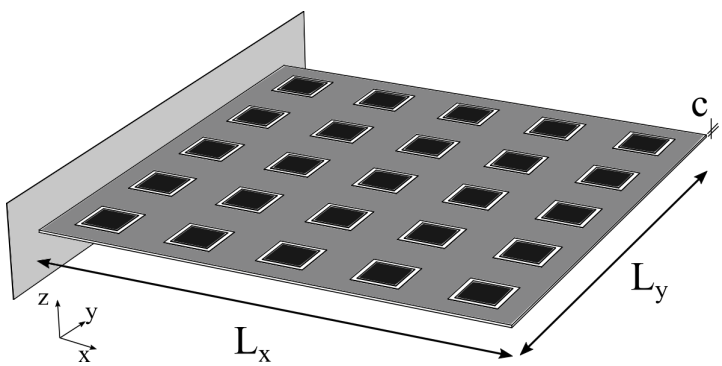

Figure 3. Cantilever plate with 20 SECs.

where b_{ij} are regression coefficients and $i > 0$ to satisfy the displacement boundary condition on the clamped edge ($w(0, y) = 0$). Considering a network with m sensors and collecting displacements at sensors' locations in a vector $\mathbf{W} \in \mathbb{R}^{m\times 1}$, the following equation can be written from equation (6)

$$\mathbf{W} = \begin{bmatrix} w_1 & \cdots & w_k & \cdots & w_m \end{bmatrix}^T = \mathbf{HB} \tag{7}$$

where $\mathbf{H} \in \mathbb{R}^{m\times n(n+1)}$ is called the location matrix and $\mathbf{B} \in \mathbb{R}^{n(n+1)\times 1}$ is the regression coefficients matrix. After straightforward computations, the following expressions are obtained for quantities contained in equation (7)

$$\mathbf{H} = \begin{bmatrix} x_1 & x_1y_1 & \cdots & x_1y_1^n & x_1^2 & x_1^2y_1 & \cdots & x_1^2y_1^n & \cdots & x_1^n & x_1^ny_1 & \cdots & x_1^ny_1^n \\ \vdots & \vdots & \vdots & \vdots & \vdots & \vdots & \vdots & \vdots & \vdots & \vdots & \vdots & \vdots & \vdots \\ x_m & x_my_m & \cdots & x_my_m^n & x_m^2 & x_m^2y_m & \cdots & x_m^2y_m^n & \cdots & x_m^n & x_m^ny_m & \cdots & x_m^ny_m^n \end{bmatrix} \tag{8}$$

$$\mathbf{B} = \begin{bmatrix} b_{10} & \cdots & b_{ij} & \cdots & b_{nn} \end{bmatrix}^T \tag{9}$$

Linear strain functions $\varepsilon_x(x,y)$ and $\varepsilon_y(x,y)$, along x and y directions, respectively, can be obtained from equation (7) by enforcing Kirchoff plate Theory as:

$$\varepsilon_x(x,y) = -\frac{c}{2}\frac{\partial^2 w(x,y)}{\partial x^2} = \mathbf{H}_x\mathbf{B}_x \tag{10}$$

$$\varepsilon_y(x,y) = -\frac{c}{2}\frac{\partial^2 w(x,y)}{\partial y^2} = \mathbf{H}_y\mathbf{B}_y \tag{11}$$

where c is the thickness of the plate. Collecting linear strains at sensors locations along x and y directions in vectors $\mathbf{E}_x$ and $\mathbf{E}_y$, respectively, and making use of equation (6), the following expressions are derived

$$\mathbf{E}_x = \mathbf{H}_x\mathbf{B}_x \tag{12}$$

$$\mathbf{E}_y = \mathbf{H}_y\mathbf{B}_y \tag{13}$$

where $\mathbf{H}_x$ and $\mathbf{H}_y$ are the location matrices for sensors transducing $\varepsilon_x(x,y)$ and $\varepsilon_y(x,y)$, respectively. Furthermore, $\mathbf{B}_x$ and $\mathbf{B}_y$ are the corresponding regression coefficients matrices. Written in terms of sensors' signals $\mathbf{S} \in \mathbb{R}^{m\times 1}$, the same equation reads:

$$\mathbf{S} = \begin{bmatrix} s_1 & \cdots & s_k & \cdots & s_m \end{bmatrix}^T = \mathbf{E}_x + \mathbf{E}_y = \mathbf{H}_s\mathbf{B}_s \tag{14}$$

where, for convenience, the signal s_k for the k-th SEC sensor is taken as:

$$s_k = \frac{\Delta C_k}{\lambda C_k} = \varepsilon_x(x_k,y_k) + \varepsilon_y(x_k,y_k) \tag{15}$$

where (x_k, y_k) denote the location of the k-th SEC sensor and $\mathbf{H}_s$ and $\mathbf{B}_s$ read as

$$\mathbf{H}_s = \left[\mathbf{H}_x | \mathbf{H}_y\right] \tag{16}$$

$$\mathbf{B}_s = \left[\frac{\mathbf{B}_x}{\mathbf{B}_y}\right] \tag{17}$$

Using sensors' readings, the regression coefficient matrix $\mathbf{B}_s$ can be estimated as $\hat{\mathbf{B}}_s$ via an LSE:

$$\hat{\mathbf{B}}_s = (\mathbf{H}_s^T\mathbf{H}_s)^{-1}\mathbf{H}_s^T\mathbf{S} \tag{18}$$

where the hat denotes an estimation. It follows that the strain maps can be reconstructed using

$$\hat{\mathbf{E}}_x = \mathbf{H}_x\hat{\mathbf{B}}_x \qquad \hat{\mathbf{E}}_y = \mathbf{H}_y\hat{\mathbf{B}}_y \tag{19}$$

However, in its unaltered form, $\mathbf{H}_s$ is multi-collinear because $\mathbf{H}_x$ and $\mathbf{H}_y$ share multiple rows, resulting in $\mathbf{H}_s^T\mathbf{H}_s$ being non-invertible. The solution utilized in [37] was to assume boundary conditions and replace selected rows of $\mathbf{H}_s$ with null coefficients or scaling factors, as determined by the particular boundary conditions. Such a strategy was numerically validated for the specialized case of a cantilever thin plate. While results demonstrated the overall promise of the algorithm, the quality of the assumptions on the boundary conditions limited the performance of the algorithm. In the section that follows, the algorithm is extended to include uni-directional data from RSGs, with the objective to minimize knowledge required on the components' boundary conditions.

3. Extended LSE-based Algorithm using HDSN

The integration of a limited number of off-the-shelf sensors within an SEC network can have the advantage to add known strain values at given locations, therefore reducing or eliminating the reliance on boundary conditions assumptions. With the proposed HDSN configurations, RSGs are introduced at strategic locations to provide accurate boundary conditions within the LSE algorithm. Data from SECs and RSGs are fused in the algorithm using the same mathematical notation, with a prime to denote quantities that are generalized in the extended algorithm. In particular, the generalized sensors' location matrix is defined as:

$$\mathbf{H}_{s'} = \left[\mathbf{\Gamma}_x \mathbf{H}_x | \mathbf{\Gamma}_y \mathbf{H}_y\right] \tag{20}$$

where $\mathbf{\Gamma}_x$ and $\mathbf{\Gamma}_y$ are appropriately defined diagonal weight matrices, as detailed in the following. The signal vector $\mathbf{S}'$, including both SEC and RSG signals, is defined as:

$$\mathbf{S}' = \left[\frac{\mathbf{S}_{\text{SEC}}}{\mathbf{S}_{\text{RSG}}}\right] \tag{21}$$

where $\mathbf{S}_{\text{SEC}}$ and $\mathbf{S}_{\text{RSG}}$ are matrices containing SEC and RSG signals, respectively. equation (18) thus becomes:

$$\hat{\mathbf{B}}' = (\mathbf{H}_{s'}^T \mathbf{H}_{s'})^{-1} \mathbf{H}_{s'}^T \mathbf{S}' \tag{22}$$

Weight matrices introduced in equation (20) are diagonal matrices composed of scalars, $\gamma_{x,k}$ and $\gamma_{y,k}$, associated with the k-th sensor. In particular, RSG signals are incorporated in $\mathbf{H}_{s'}$ using

$$\gamma_{x,k} = 1 \ , \ \gamma_{y,k} = 0 \tag{23}$$

when the k-th RSG measures strain along the x-axis only, or, alternatively,

$$\gamma_{x,k} = 0 \ , \ \gamma_{y,k} = 1 \tag{24}$$

when the k-th RSG measures strain along the y-axis only. Different weight values other than unity can be selected in the design to add more importance to particular sensors. For instance, $\gamma > 1$ can be selected for RSGs due to their high level of accuracy compared with the SEC technology, or for SECs installed along a known boundary condition.

The extended algorithm also includes virtual sensors based on knowledge about the system's behavior. Virtual sensors are analogous to assumed boundary conditions, except that they are located at points on the edge of the strain reconstruction map. In the algorithm, virtual sensors are treated identically to RSGs and can also be used directly in the reconstruction of the strain maps. For instance, a sensor reading $\varepsilon_y = 0$ can be added under a clamped fixity that extends along the y axis.

The extended LSE-based algorithm is conceptually illustrated in figure 4. Dotted boxes in the figure represent the two new features added through the utilization of an HDSN. Both the virtual sensors and RSG signals can be utilized either fully or partly

into the LSE or directly in the reconstruction of the strain maps as known points. Strain maps are decomposed at the sensors' locations included in matrix $\mathbf{H}_{s'}$ and reconstructed elsewhere using C^2 continuous biharmonic splines. The algorithm can be specified by constructing splines that interpolate decomposed strains from equation (19), strains measured by RSGs and/or strains known at virtual sensors locations.

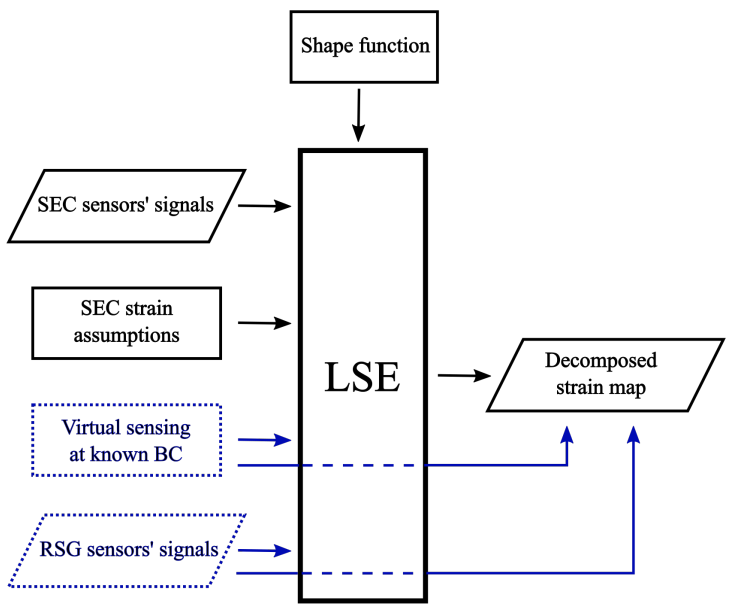

Figure 4. Modified strain decomposition algorithm.

The described extended algorithm still includes boundary conditions on the SEC strain readings, as it was the case for the original algorithm, to provide the user with greater flexibility. For instance, in the case of a cantilever plate, the boundary condition along the fixity can be assumed as $\varepsilon_y(0, a_y \leq y \leq L_y - a_y) = 0$, where a_y is a positive constant such that $0 \leq a_y \leq L_y/2$ to account for different boundary conditions at corners. This assumed boundary condition is enforced for SECs installed along the fixity using $\gamma_{x,m} = 1$, $\gamma_{y,m} = 0$.

4. Methodology

Validation of the strain decomposition algorithm presented in Section 3 is conducted experimentally on an HDSN. This section describes the methodology used for the experimental validation.

4.1. HDSN configuration

The HDSN consists of 20 SECs and 46 RSGs deployed onto the surface of a fiberglass plate of geometry $74 \times 63 \times 0.32$ cm^3 fixed along one edge with clamps as shown in

figure 5(a). Figure 5(b) is a schematic of the SEC and RSG sensor placement. Each SEC covers $6.5 \times 6.5 = 42$ cm^2 in area, laid out in a 4×5 grid array. The point node used in constructing the $\mathbf{H}_{\mathbf{s}'}$ matrix is taken as the center of each SEC. RSGs used in the experimental setup are foil-type strain gauges of 6 mm length manufactured by Tokyo Sokki Kenkyujo, model FLA-6-350-11-3LT. They are aligned along the directions of the plate's edges, in either a single or double configuration, individually measuring ε_x and ε_y as indicated in figure 5(b) by using circles and squares, respectively. The number of considered RSGs was purposely very large in order to provide enough measurement points to assess the performance of the algorithm as a function of the number of arbitrarily located RSGs.

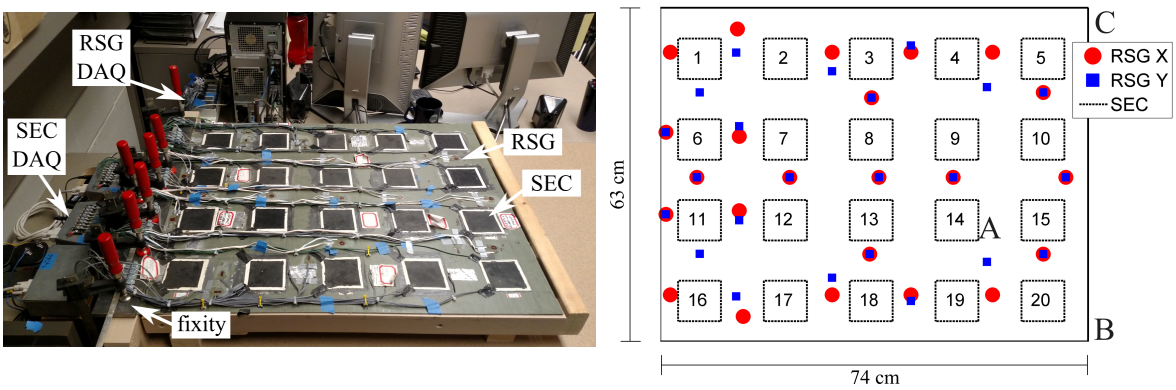

(a) (b)

Figure 5. (a) Picture of the experimental configuration; and (b) sensor nomenclature.

The plate is subjected to four different displacement-controlled load cases, listed in Table 1. Load case I consists of an upward uniform displacement along the free edge $\overline{\mathrm{BC}}$ as shown in figure 5(b). Load case II is a downward uniform displacement along free edge $\overline{\mathrm{BC}}$. Load case III is an upward point displacement under point A (directly under SEC 14), with points B and C restrained in the vertical direction. Load case IV consists of an upward displacement at point C, with point B restrained in the vertical direction. The displacement controlled loads were applied using a frame built from extruded aluminum framing. Each test consisted of three 15-second sets of unloaded, loaded, and unloaded conditions, for a total of 45 seconds.

Table 1. Loading cases.

loading case	point of applied displacement	displacement (mm)	vertical displacement restraints
I	$\overline{\mathrm{BC}}$	125	none
II	$\overline{\mathrm{BC}}$	-97	none
III	A	47	B,C
IV	C	47	B

Different data acquisition (DAQ) hardware is used for the measurement of the SEC and RSG sensors, as annotated in figure 5(a). SEC measurements are recorded using a capacitance-to-digital converter, PCAP-02, mounted inside protective boxes and manufactured by ACAM-Messelectronic GmbH. Capacitance measurement is performed by measuring the SEC sensors discharge time, in comparison with the discharge time of a known reference capacitor. This DAQ is capable of reading up to 7 channels, multiplexed though a single capacitance-to-digital converter. The acquisition of data was performed using a PCAP-02 evaluation board with ACAM's evaluation software at a sampling rate of 25 Hz. RSG measurements are recorded using a National Instruments cDAQ-9174 with four 24-bit 350 Ω quarter-bridge modules (NI-9236) through LabVIEW, sampled at 100 Hz.

Figure 6 shows an example of SEC signal, ΔC, acquired from a row of sensors (16 - 20) during load case III. Data are presented filtered using a moving average. The sensors operate as designed under both compression and tension. Given the static nature of the study, the capacitance signal for the reconstruction of strain maps is taken as the average of data points between 23 and 28 seconds.

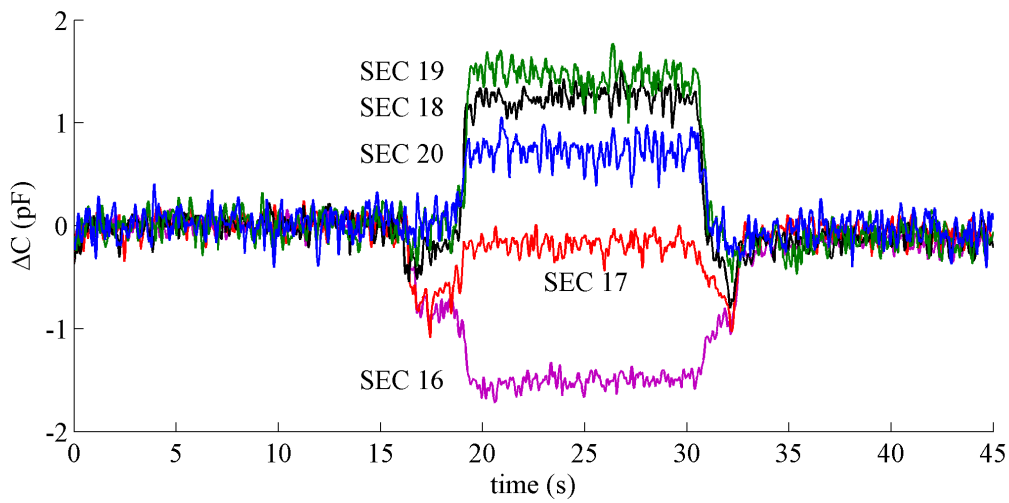

Figure 6. Example of sensor signals: sensors SEC 16-20 under load case III.

4.2. Algorithm Configurations

Validation is performed on different algorithm configurations, as listed in Table 2, to investigate the effects of the different inputs illustrated in the block diagram of figure 4. Algorithm 1 consists of enforcing boundary conditions through the introduction of RSGs into the SEC DSN, forming an HDSN. This is obtained by adding RSGs into $\mathbf{H}_{s'}$. Algorithms 2-4 add additional inputs, namely virtual sensors at known boundary conditions, assumptions on the SEC strain boundary conditions and RSG data directly

in the reconstruction of the strain maps. Algorithm 5 uses all the inputs.

Table 2. Evaluated algorithm configurations.

algorithm configuration	virtual sensing	SEC assumptions	RSG data in strain maps	RSGs added into $\mathbf{H}_{s'}$
1				x
2	x			x
3		x		x
4			x	x
5	x	x	x	x

For the thin plate under study, virtual sensors are added to enforce the assumptions on the boundary conditions. On the fixed edge, $\varepsilon_y = 0$ is assumed for $a_y \leq y \leq L_y - a_y$ where $a_y = 5$ mm to account for the corner effects. For all loading cases, 5 virtual sensors are placed along the fixity ($x = 0$) at $y = 5.00$, 15.8, 26.6, 37.4, 48.2 and 59.0 mm with virtual signals $\varepsilon_y = 0$. For the purpose of enforcing the plates boundary conditions, and due to low levels of ε_x along the free edge opposite to the fixity, the assumption that $\varepsilon_x \approx 0$ was made along the free edge. Five virtual sensors are placed along the free edge ($x = 0.74$ mm) at $y = 5.00$, 15.8, 26.6, 37.4, 48.2 and 59.0 mm with signals ($\varepsilon_x = 0$). While this assumption is valid only for load cases 1 and 2, it has shown to be convenient to equate the strain levels to 0 given the low levels of strain at these positions.

For the algorithm cases based on strain assumptions at the SECs locations, different assumptions were made along the plate's edges for different load cases in order to be consistent with the prior form of the algorithm. For the boundary conditions along the fixity, ε_y was assumed to be zero for $a_y \leq y \leq L_y - a_y$, where a_y is taken as 20 cm. This is enforced in the LSE algorithm by setting $\gamma_{y,11} = 0$ and $\gamma_{y,16} = 0$. A similar approach was taken for ε_x at the plate's free edge (SEC 10 and 15) due to the low level of strain present, ε_x was enforced as zero by setting $\gamma_{x,10} = 0$ and $\gamma_{x,15} = 0$. Under the asymmetric loads (loading cases III and IV), different assumptions are conducted on ε_x and ε_y. Table 3 summarizes weights used to enforce the assumptions on boundary conditions for all SECs under different loading cases.

Table 3. Weight parameters γ used to enforce the assumptions on boundary conditions.

	loading case							
	I		II		III		IV	
SEC	γ_x	γ_y	γ_x	γ_y	γ_x	γ_y	γ_x	γ_y
1	1	1	1	1	1	0	1	1
2 to 5	1	1	1	1	1	1	1	1
6	1	0	1	0	1	0	1	0
7 to 9	1	1	1	1	1	1	1	1
10	0	1	0	1	1	1	0	1
11	1	0	1	0	1	0	1	0
12 to 14	1	1	1	1	1	1	1	1
15	0	1	0	1	1	1	0	1
16	1	1	1	1	1	0	1	1
17 to 20	1	1	1	1	1	1	1	1

For the algorithm cases utilizing RSG data directly in the strain maps, RSG sensor data are introduced directly into the decomposed strain maps alongside with the decomposed SEC strains from the enhanced LSE algorithm. Lastly, for all of the algorithms, a polynomial function (equation (6)) for the deflection shape was assumed. A fourth order polynomial was selected to improve the ability of the strain decomposition algorithm in capturing more complex strain features in the y direction. Note that $i \geq 2$ and $j \geq 2$ to satisfy the boundary conditions of a cantilever plate.

$$w(x, y) = \sum_{i=2,j=2}^{4} a_{ij} x^i y^j \tag{25}$$

4.3. Selection of RSGs into the HDSN

Selection of the RSGs is conducted randomly to study the influence of sensor placement on the performance of the algorithm. A total of 100 sets of randomly selected sensors constructed from the RSG placement shown in figure 5(b) were generated. Simulations consist of adding RSGs in the HDSN in the order listed in each random set. Each algorithm case is ran 100 times, and results show the average value of the LSE performance. The variance in performance under changing RSGs sensors layout is also discussed. The special case of 1 single RSG, for which only 46 permutations are possible, is not considered. Optimal sensor placement for RSGs within the HDSN is out-of-the-scope of this paper.

5. Results

Results from the experimental validation are presented and discussed in this section. The performance of each algorithm configuration (Table 2) is quantified using the mean absolute error (MAE) between the LSE estimated strain maps and the known strains at the locations of the RSGs (23 along the x-axis and 23 along the y-axis). The LSE estimated strain maps are developed for the entire area of the cantilever plate shown in figure 5. In the subsection that follows, the performance in strain reconstruction is investigated, for different LSE-based algorithms, as a function of the number of RSGs used in the algorithm, taken at random locations as discussed in Section 4. Afterward, the robustness of the algorithm is studied as a function of RSG sensor placement.

5.1. Algorithm Configurations

Figure 7 shows the average performance of the algorithms under each loading case. The "RSG-only" case is the performance benchmark, and converges to 0 as the number of RSG augments due to the formulation of the MAE index. As expected, the performance of each algorithm improves with the number of RSGs used into the HDSN. Using algorithm 1 as the base line (simplest form), algorithms 2-5 improve on the MAE to various levels, where adding more inputs to the algorithms helps the reconstruction of strain maps, except for a few cases (loading case I, for instance) where algorithm 3 underperforms algorithm 1, most likely due to errors on the boundary conditions assumptions. Algorithm 2 provides a substantial improvement in the MAE compared with algorithm 1 through the integration of virtual sensors. Algorithm 4 generally exhibits a slower convergence rate, offering only a marginal improvement to the base LSE algorithm (algorithm 1). However, algorithm 4 could see substantial improvement with an optimized sensor placement scheme. Lastly, algorithm 5, which combines all of the inputs, performs similarly to algorithm 2. Under most loading conditions and algorithms configurations, the extended LSE algorithm provides a better representation of the unidirectional strain maps than the equivalent number of RSGs, when less than 20 RSGs are added into the HDSN, demonstrating a net advantage of utilizing an HDSN. Also, it can be concluded from these results that algorithm 2 offers the best performance given its simplicity. Another notable advantage of algorithm 2 over algorithm 5 is that it does not include SEC assumptions, which need to be adjusted depending upon the peculiar loading condition. It is, therefore, a generally applicable algorithm.

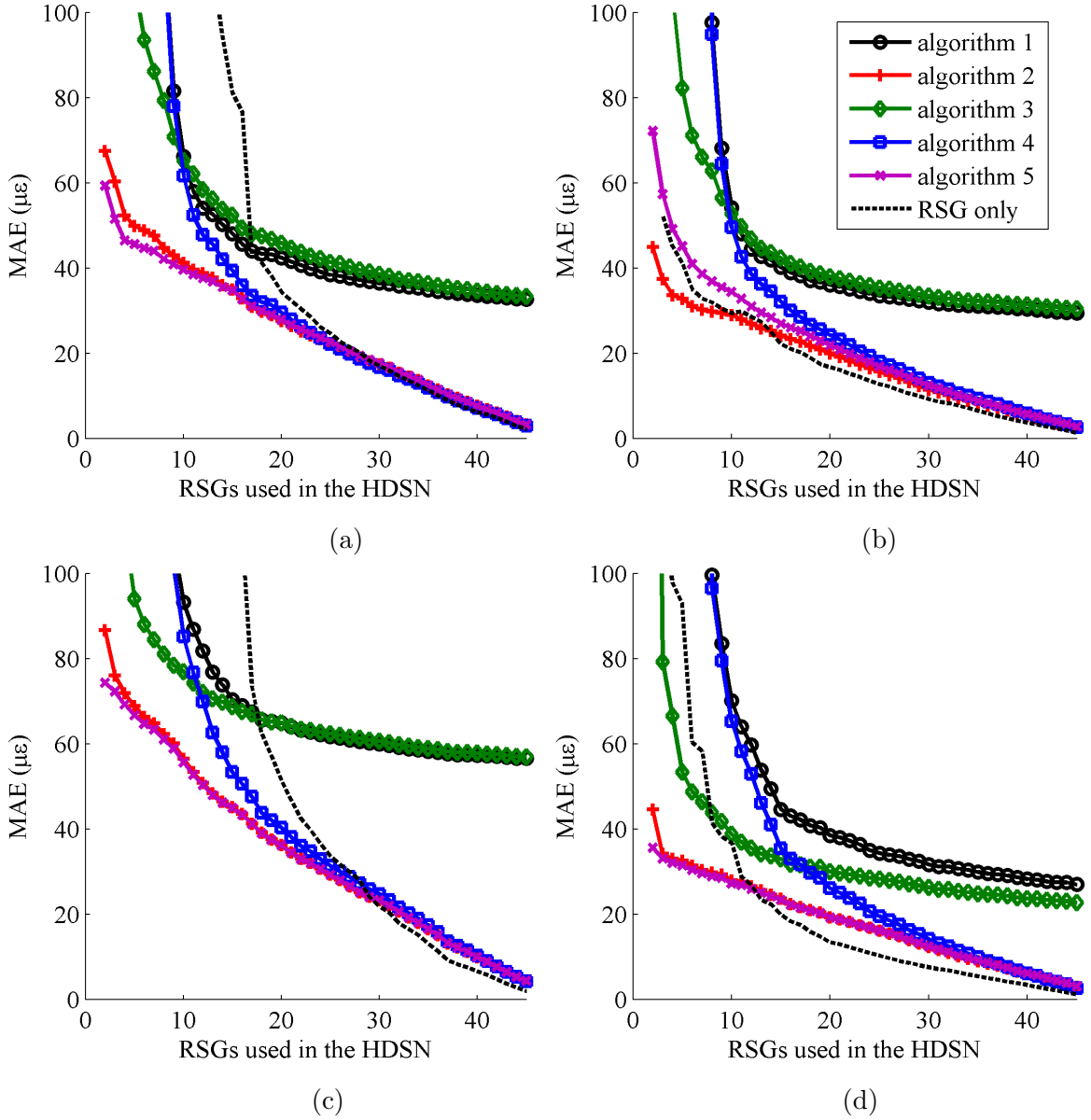
MAE (με)
RSGs used in the HDSN
algorithm 1
algorithm 2
algorithm 3
algorithm 4
algorithm 5
RSG only
(a)
(b)
(c)
(d)

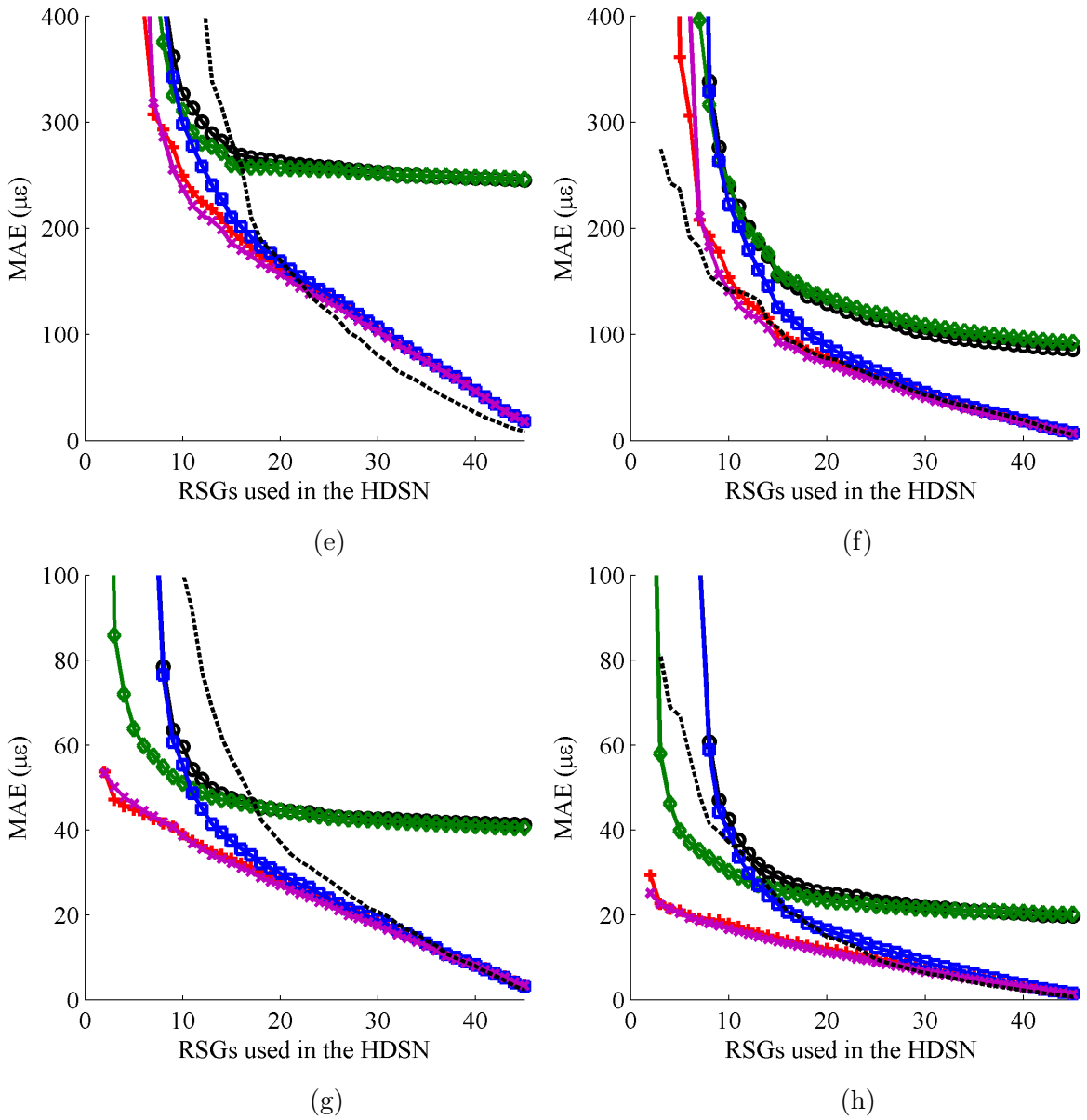

Figure 7. Algorithm results for varying RSGs added to the DSN: (a) load case I for ε_x; (b) load case I for ε_y; (c) load case II for ε_x; (d) load case II for ε_y; (e) load case III for ε_x; (f) load case III for ε_y; (g) load case IV for ε_x; and (h) load case IV for ε_y.

The decomposed strain maps are presented in figure 8. An HDSN consisting of 20 RSGs was arbitrarily selected to investigate the extended LSE algorithm (configuration 2) when using an equal number of RSGs and SECs. The decomposed strain maps are compared against the strain maps obtained using 46 RSGs only. The layout of RSG sensors within the HDSN was selected to provide the best fit from the list of 100 randomly generated sensor placement arrangements discussed in Section 4.3. Results show similar maps, with slight disagreements for the strain along the y-axis. Obtaining a more accurate fit for ε_y would require a higher order shape function. Such strategy was not investigated due to the low number of SECs along that axis, which would result

in over-fitting for lower numbers of RSGs used into the HDSN.

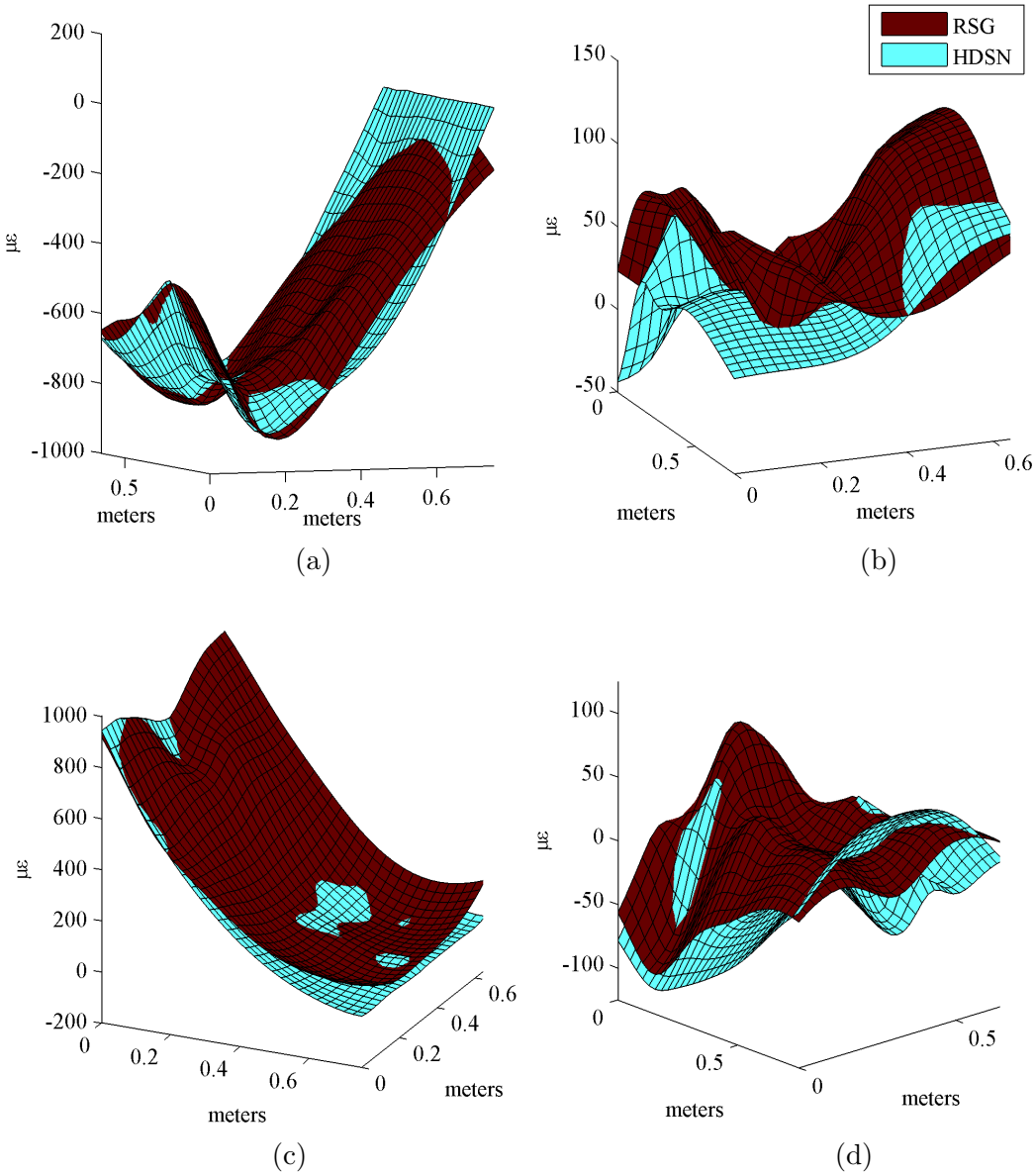

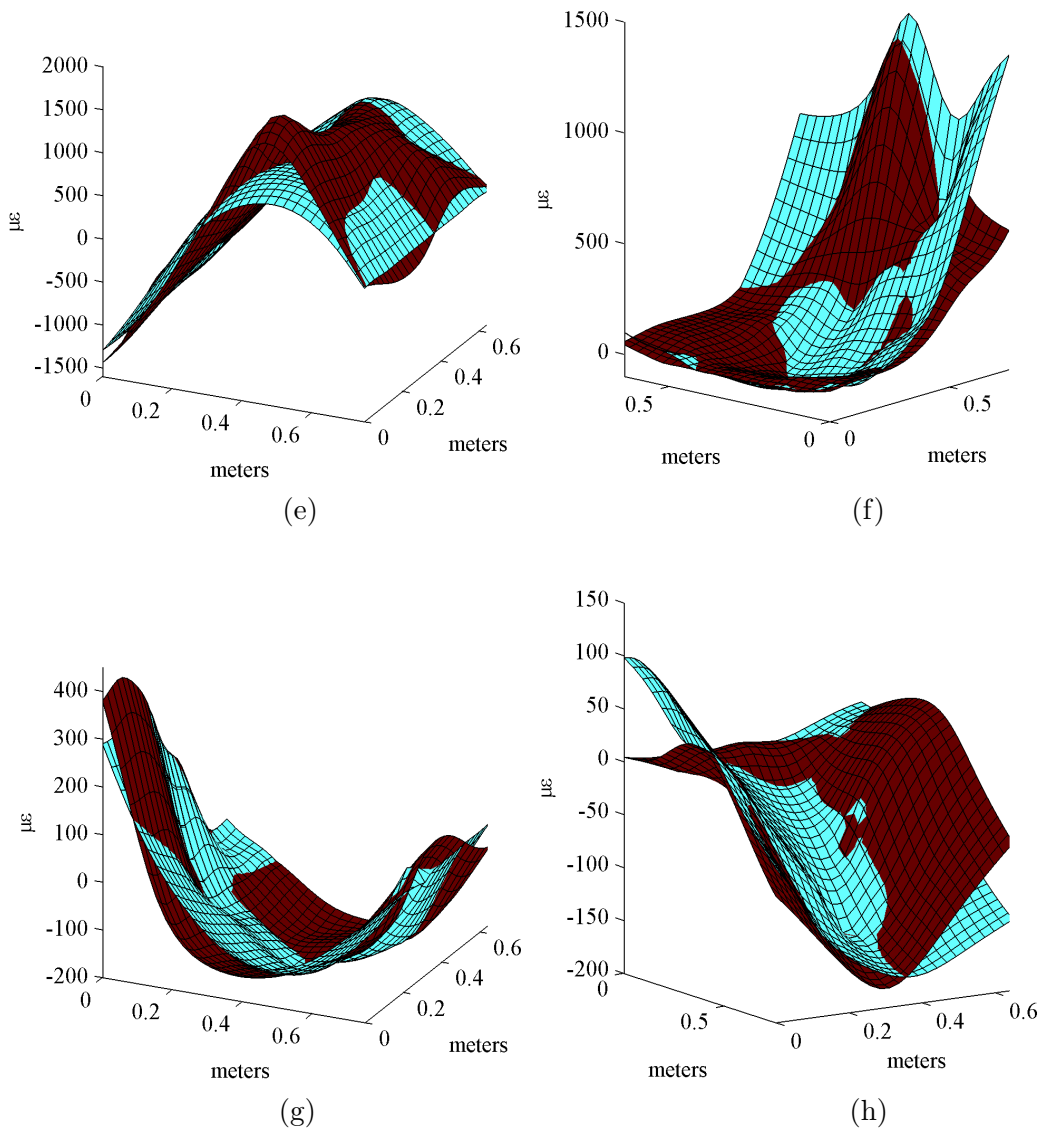

Figure 8. Decomposed strain maps: (a) load case I for ε_x; (b) load case I for ε_y; (c) load case II for ε_x; (d) load case II for ε_y; (e) load case IV for ε_x; (f) load case III for ε_y; (g) load case IV for ε_x; and (h) load case IV for ε_y.

5.2. Algorithm robustness to sensor placement

The robustness of the LSE-based algorithm with respect to the layout of RSG sensors is evaluated by comparing the 95% confidence bound on the MAE over all 100 sensor placement cases. For the study, algorithm 2 is selected due to its higher overall performance compared with other algorithm variations. Figure 9 compares the results with the RSG only case. Except for loading case III, the 95% confidence bound on the HDSN using algorithm 2 is small compared to the 95% confidence bound using RSGs only. This is as expected, given that the HDSN always utilizes 20 SECs spread over the entire plate. The 95% confidence bound is larger for loading case III, most likely due

to the higher complexity of the strain maps. Overall, the confidence bounds obtained by the HDSN are tighter than those obtained using RSG readings only, which allows the authors to conclude that the HDSN has a high robustness with respect to sensor placement.

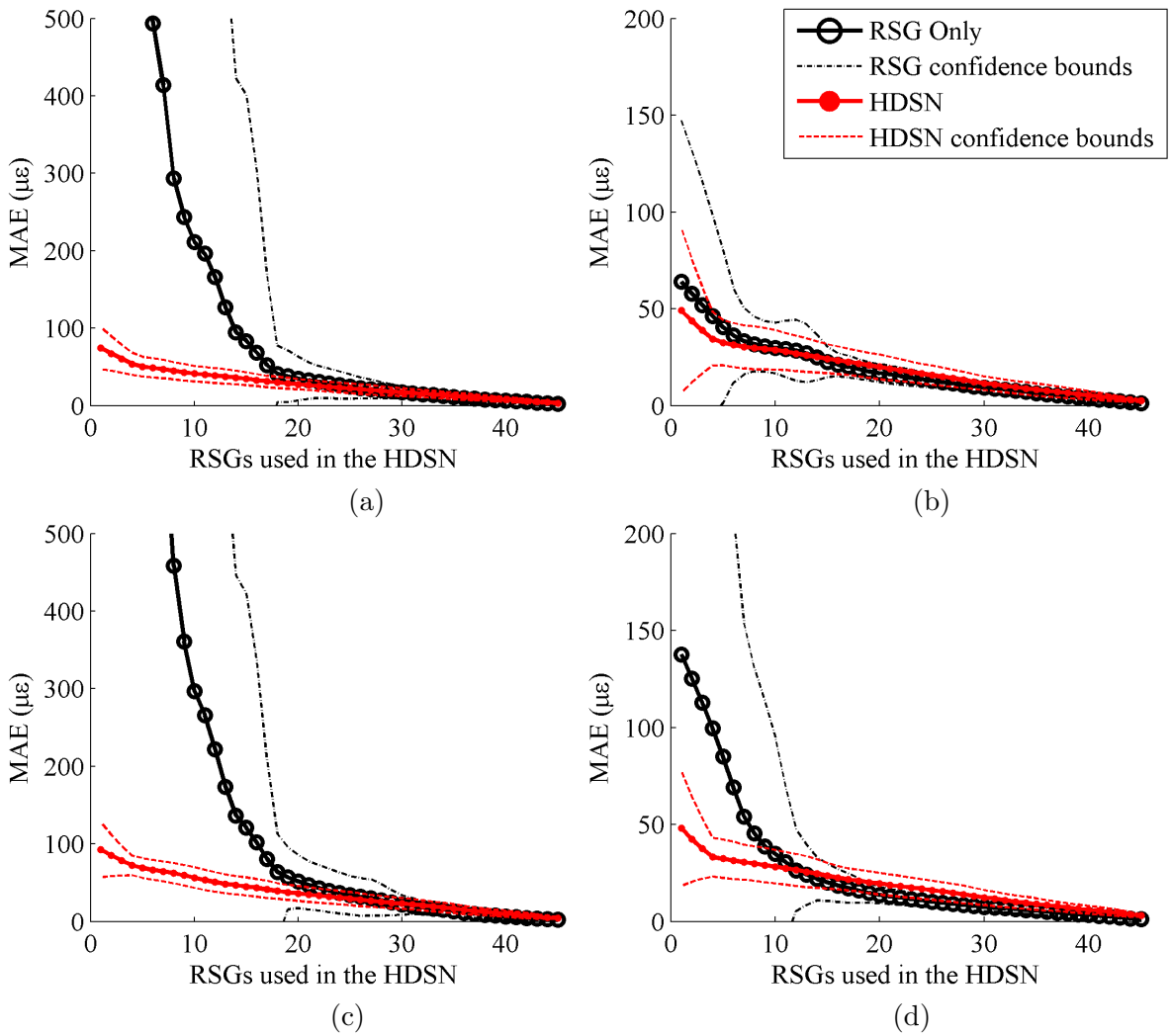

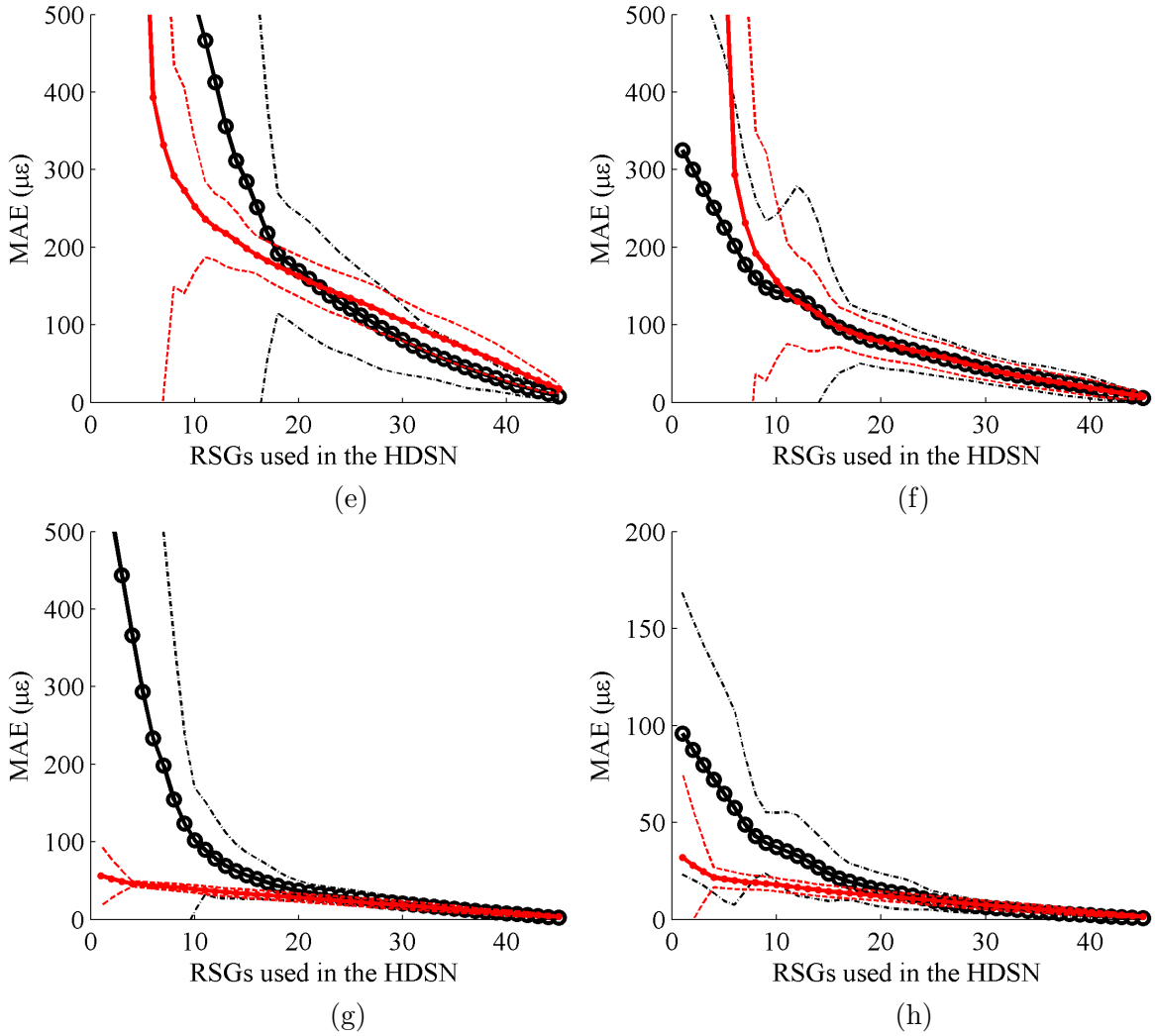

Figure 9. Algorithm robustness towards sensor placement: (a) load case I for ε_x; (b) load case I for ε_y; (c) load case II for ε_x; (d) load case II for ε_y; (e) load case III for ε_x; (f) load case III for ε_y; (g) load case IV for ε_x; and (h) load case IV for ε_y.

6. Conclusion

This paper presented a method for the directional decomposition of additive strain measured by a novel large soft elastomeric capacitor (SEC). The SEC is an inexpensive strain gauge, designed to cover large surfaces for the purpose of damage detection and localization. A previously proposed least squares estimator (LSE)-based algorithm was enhanced to provide boundary condition updating though the use of a hybrid dense network (HDSN) leveraging mature off-the-shelf technology, in particular, a set of electrical resistive strain gauges (RSGs). In this HDSN configuration, the SECs' ability to inexpensively monitor large areas is combined with the RSGs ability to provide precise, unidirectional local strain measurements. The original LSE algorithm consists of assuming a shape function in the framework of classical Kirchhoff plate theory and using an LSE to find the coefficients of the shape function. The enhanced LSE algorithm

introduces weighted matrices to concatenate and achieve an effective fusion between signals from both the SECs and the RSGs. Additionally, virtual sensing nodes are introduced along the plates known boundary conditions to enforce known boundary conditions outside the HDSN sensing points.

Experimental investigations were conducted on a cantilever plate equipped with 20 SECs and 46 RSGs. For a plate under simple loading cases, the LSE algorithm successfully produced unidirectional strain maps. However, it showed limitations in fitting more complex strain fields, possibly due to the limited number of sensors (SECs and RSGs) used in the investigation that limited the order of the polynomial used in representing the shape function. Further investigation is needed to validate the proposed algorithm for use with different HDSN layouts and with an expanded library of loading cases. While the proposed strategy showed to be robust with respect to sensor placement, the formal network design, including the optimal placement, type, and number of sensors within an HDSN needs to be explored. The algorithmic improvements presented here build a basis for future work in real-time boundary condition updating and regression fitting of parameters' weights.

Acknowledgments

The development of the SEC technology is supported by grant No. 13-02 from the Iowa Energy Center. This work is also partly supported by the National Science Foundation Grant No. 1069283, which supports the activities of the Integrative Graduate Education and Research Traineeship (IGERT) in Wind Energy Science, Engineering and Policy (WESEP) at Iowa State University. Their support is gratefully acknowledged.

[1] Simon Laflamme, Filippo Ubertini, Hussam Saleem, Antonella DAlessandro, Austin Downey, Halil Ceylan, and Annibale Luigi Materazzi. Dynamic characterization of a soft elastomeric capacitor for structural health monitoring. *Journal of Structural Engineering*, 141(8):04014186, 2015.

[2] Peter C Chang, Alison Flatau, and SC Liu. Review paper: health monitoring of civil infrastructure. *Structural health monitoring*, 2(3):257–267, 2003.

[3] Chia Chen Ciang, Jung-Ryul Lee, and Hyung-Joon Bang. Structural health monitoring for a wind turbine system: a review of damage detection methods. *Measurement Science and Technology*, 19(12):122001, 2008.

[4] Douglas Adams, Jonathan White, Mark Rumsey, and Charles Farrar. Structural health monitoring of wind turbines: method and application to a hawt. *Wind Energy*, 14(4):603–623, 2011.

[5] Y Zou, LPSG Tong, and GP Steven. Vibration-based model-dependent damage (delamination) identification and health monitoring for composite structuresa review. *Journal of Sound and vibration*, 230(2):357–378, 2000.

[6] Filippo Ubertini, Annibale Luigi Materazzi, Antonella DAlessandro, and Simon Laflamme. Natural frequencies identification of a reinforced concrete beam using carbon nanotube cement-based sensors. *Engineering structures*, 60:265–275, 2014.

[7] Erik Gross, Todd Simmermacher, Mark Rumsey, and Rick I Zadoks. Application of damage detection techniques using wind turbine modal data. In *American Society of Mechanical Engineers Wind Energy Symp.(Reno, NV, USA)*, pages 99–0047, 1999.

[8] Mark A Rumsey and Joshua A Paquette. Structural health monitoring of wind turbine blades. In *The 15th International Symposium on: Smart Structures and Materials & Nondestructive Evaluation and Health Monitoring*, pages 69330E–69330E. International Society for Optics and Photonics, 2008.

[9] Chia Chen Ciang, Jung-Ryul Lee, and Hyung-Joon Bang. Structural health monitoring for a wind turbine system: a review of damage detection methods. *Measurement Science and Technology*, 19(12):122001, 2008.

[10] Dan M Frangopol and Thomas B Messervey. Life-cycle cost and performance prediction: role of structural health monitoring. *Frontier technologies for infrastructures engineering: structures and infrastructures book series*, 4:361, 2009.

[11] John A Rogers, Takao Someya, and Yonggang Huang. Materials and mechanics for stretchable electronics. *Science*, 327(5973):1603–1607, 2010.

[12] Hyung-Kew Lee, Sun-Il Chang, and Euisik Yoon. A flexible polymer tactile sensor: fabrication and modular expandability for large area deployment. *Microelectromechanical Systems, Journal of*, 15(6):1681–1686, 2006.

[13] Yong Xu, Fukang Jiang, Scott Newbern, Adam Huang, Chih-Ming Ho, and Yu-Chong Tai. Flexible shear-stress sensor skin and its application to unmanned aerial vehicles. *Sensors and Actuators A: Physical*, 105(3):321–329, 2003.

[14] Mariwan Ahmed, Ismail Erkin Gonenli, Gaviraj S Nadvi, Rohit Kilaru, Donald P Butler, and Zeynep Celik-Butler. Mems sensors on flexible substrates towards a smart skin. In *Sensors, 2012 IEEE*, pages 1–4. IEEE, 2012.

[15] Md Sohel Mahmood, Zeynep Celik-Butler, and Donald P Butler. Design and fabrication of self-packaged, flexible mems accelerometer. In *SENSORS, 2015 IEEE*, pages 1–4. IEEE, 2015.

[16] Yingzhe Hu, Warren S Rieutort-Louis, Josue Sanz-Robinson, Liechao Huang, Branko Glisic, James C Sturm, Steffen Wagner, Naveen Verma, et al. Large-scale sensing system combining large-area electronics and cmos ics for structural-health monitoring. *Solid-State Circuits, IEEE Journal of*, 49(2):513–523, 2014.

[17] ST Tung, Y Yao, and B Glisic. Sensing sheet: the sensitivity of thin-film full-bridge strain sensors for crack detection and characterization. *Measurement Science and Technology*, 25(7):075602, 2014.

[18] Inpil Kang, Mark J Schulz, Jay H Kim, Vesselin Shanov, and Donglu Shi. A carbon nanotube strain sensor for structural health monitoring. *Smart Materials and Structures*, 15(3):737, 2006.

[19] Neng-Kai Chang, Chi-Chung Su, and Shuo-Hung Chang. Fabrication of single-walled carbon nanotube flexible strain sensors with high sensitivity. *Applied Physics Letters*, 92(6):063501, 2008.

[20] S Grilli, S Coppola, V Vespini, V Pagliarulo, G Nasti, C Carfagna, and P Ferraro. One-step fabrication of free-standing flexible membranes reinforced with self-assembled arrays of carbon nanotubes. *Applied Physics Letters*, 105(15):153101, 2014.

[21] Darren J Lipomi, Michael Vosgueritchian, Benjamin CK Tee, Sondra L Hellstrom, Jennifer A Lee, Courtney H Fox, and Zhenan Bao. Skin-like pressure and strain sensors based on transparent elastic films of carbon nanotubes. *Nature nanotechnology*, 6(12):788–792, 2011.

[22] Andrew R Burton, Masahiro Kurata, Hiromichi Nishino, and Jerome P Lynch. Fully integrated patterned carbon nanotube strain sensors on flexible sensing skin substrates for structural health monitoring. In *SPIE Smart Structures and Materials+ Nondestructive Evaluation and Health Monitoring*, pages 98030S–98030S. International Society for Optics and Photonics, 2016.

[23] Takeo Yamada, Yuhei Hayamizu, Yuki Yamamoto, Yoshiki Yomogida, Ali Izadi-Najafabadi, Don N Futaba, and Kenji Hata. A stretchable carbon nanotube strain sensor for human-motion detection. *Nature nanotechnology*, 6(5):296–301, 2011.

[24] Michael Suster, Jun Guo, Nattapon Chaimanonart, Wen H Ko, and Darrin J Young. A high-performance mems capacitive strain sensing system. *Microelectromechanical Systems, Journal of*, 15(5):1069–1077, 2006.

[25] Bo-Yeon Lee, Jiyoon Kim, Hyungjin Kim, Chiwoo Kim, and Sin-Doo Lee. Low-cost flexible pressure sensor based on dielectric elastomer film with micro-pores. *Sensors and Actuators A: Physical*, 240:103–109, 2016.

[26] Jagoda Anna Dobrzynska and MAM Gijs. Polymer-based flexible capacitive sensor for three-axial force measurements. *Journal of Micromechanics and Microengineering*, 23(1):015009, 2012.

[27] Wangchang Geng, Xiaowei He, Yuanwei Su, Jing Dang, Junwei Gu, Wei Tian, and Qiuyu Zhang. Remarkable humidity-responsive sensor based on poly (n, n-diethylaminoethyl methacrylate)-b-polystyrene block copolymers. *Sensors and Actuators B: Chemical*, 226:471–477, 2016.

[28] PM Harrey, BJ Ramsey, PSA Evans, and DJ Harrison. Capacitive-type humidity sensors fabricated using the offset lithographic printing process. *Sensors and Actuators B: Chemical*, 87(2):226–232, 2002.

[29] Christian Metzger, Elgar Fleisch, Jan Meyer, Mario Dansachmüller, Ingrid Graz, Martin Kaltenbrunner, Christoph Keplinger, Reinhard Schwödiauer, and Siegfried Bauer. Flexible-foam-based capacitive sensor arrays for object detection at low cost. *Applied Physics Letters*, 92(1):013506, 2008.

[30] Ryuichiro Yoda. Elastomers for biomedical applications. *Journal of Biomaterials Science, Polymer Edition*, 9(6):561–626, 1998.

[31] S. Laflamme, H.S. Saleem, B.K. Vasan, R.L. Geiger, Degang Chen, M.R. Kessler, and K. Rajan. Soft elastomeric capacitor network for strain sensing over large surfaces. *Mechatronics, IEEE/ASME Transactions on*, 18(6):1647–1654, Dec 2013.

[32] Simon Laflamme, Matthias Kollosche, Jerome J Connor, and Guggi Kofod. Robust flexible capacitive surface sensor for structural health monitoring applications. *Journal of Engineering Mechanics*, 139(7):879–885, 2012.

[33] Hussam Saleem, Austin Downey, Simon Laflamme, Matthias Kollosche, and Filippo Ubertini. Investigation of dynamic properties of a novel capacitive-based sensing skin for nondestructive testing. *Materials Evaluation*, 73(10):1390–1397, 2015.

[34] S Laflamme, L Cao, E Chatzi, and F Ubertini. Damage detection and localization from dense network of strain sensors. *Shock and Vibration*, 2016(2562949):1–13, 2016.

[35] F Ubertini and F Giuliano. Computer simulation of stochastic wind velocity fields for structural response analysis: Comparisons and applications. *Advances in Civil Engineering*, 2010(749578):1–20, 2010.

[36] Sari Kharroub, Simon Laflamme, Chunhui Song, Daji Qiao, Brent Phares, and Jian Li. Smart

sensing skin for detection and localization of fatigue cracks. *Smart Materials and Structures*, 24(6):065004, 2015.

[37] Jingzhe Wu, Chunhui Song, Hussam S Saleem, Austin Downey, and Simon Laflamme. Network of flexible capacitive strain gauges for the reconstruction of surface strain. *Measurement Science and Technology*, 26(5):055103, 2015.

[38] Wenyi Liu, Baoping Tang, and Yonghua Jiang. Status and problems of wind turbine structural health monitoring techniques in china. *Renewable Energy*, 35(7):1414–1418, 2010.

[39] A.N. Wilkinson, M.L. Clemens, and V.M. Harding. The effects of sebs-g-maleic anhydride reaction on the morphology and properties of polypropylene/pa6/sebs ternary blends. *Polymer*, 45(15):5239 – 5249, 2004.